

Fiber Bragg grating sensor for two-phase flow in microchannels

Nigel David · Ned Djilali · Peter Wild

Received: 4 November 2011 / Accepted: 20 January 2012 / Published online: 14 February 2012
© Springer-Verlag 2012

Abstract A new non-intrusive measurement technique for two-phase flow in microchannels is presented. The development of an evanescent field-based optical fiber Bragg grating (FBG) sensor is described, and experiments coupled with flow visualization demonstrating the performance of this sensor are presented. Two adjacent 1-mm FBGs in etched D-shaped fiber are embedded into the surface of a PDMS microchannel. Experiments are conducted in both droplet and slug flow regimes and high-speed digital video is captured synchronously with the sensor data. The FBGs exhibit an on–off type response to the passage droplets which is shown to correlate precisely with the passage of the liquid phase. This correlation enables the measurement of droplet average velocity and size using only the sensor data. In addition to the use of both FBG signals for the purpose of measuring droplet speed and size, it is shown that for droplets larger than the FBG length, a single FBG can be used to estimate the convection velocity and size of fast moving droplets. This sensing method is potentially useful for monitoring two-phase flow in fuel cells and microfluidic applications such as micro-heat exchangers and lab-on-a-chip systems.

Keywords Multiphase flow · Liquid water · Fiber-optics · PEM fuel cell · Water management

1 Introduction

Two phase flows in microchannels occur in numerous applications. These include heat sinks that rely on the phase transition of boiling refrigerants to cool integrated circuits and electronic devices (Hetsroni et al. 2002; Zhang et al. 2002), microfluidic devices used in microchemical microelectromechanical and lab-on-chip systems (Gunther et al. 2004; Funfschilling et al. 2010), and fuel cells used to convert chemical energy into electricity (Zhu et al. 2008a). In spite of the progress in general understanding of microchannel two-phase flow phenomena, the development of broadly applicable predictive models is still lagging. Two-phase flow regimes in microchannels differ significantly (Bergles 2005; Waelchli and Von Rohr 2006; Zhu et al. 2008b) from those encountered in more classical systems, and there is a need for improved experimental techniques (Tibiri 2010) to further fundamental understanding of flow dynamics, bubble and/or film sizes, pressure drop, wettability, etc. to inform improved design and control of the flow and associated transport processes. In polymer electrolyte membrane (PEM) fuel cells, which are the primary motivation for the work presented here, liquid water management in the gas flow microchannels is a critical problem that leads to numerous performance and material degradation issues (Bazylak 2009; Li et al. 2008). In microfluidic devices that are increasingly designed for an array of complex processes including mixing, assays and chemical reactions, more precise understanding of the dynamics of immiscible fluid phases is needed to achieve precise control (Schembri 2011).

Experimental methods currently available for characterizing the dynamics and mixing of two-phase flows in microchannels and micro-reactors are reviewed in King (2007). These include visualization techniques tracking

N. David · N. Djilali (✉) · P. Wild
Department of Mechanical Engineering,
Institute for Integrated Energy Systems,
University of Victoria, PO Box 3055, STN CSC,
Victoria, BC V8W 3P6, Canada
e-mail: ndjilali@uvic.ca

directly interfaces or in conjunction with fluorescent dyes or reactive species; micro particle image velocimetry; and non-intrusive sensors. Visualization techniques have also been extensively used to visualize liquid water in operating fuel cells (Bazylak 2009) specifically designed to allow optical access; the techniques include NMR imaging, neutron imaging, synchrotron X-ray imaging, microtomography and optical photography. Visualization-based techniques have proven extremely valuable but typically require expensive equipment, and are limited to optically accessible systems. Investigation of multi-layered microfluidic devices is for example difficult, and optical access in commercial fuel cell stacks is not possible without compromising the design.

Micro-sensors are an obvious alternative to address the needs for monitoring and measurements. Non-intrusive sensors that rely on infrared absorption or refractive index detection have been developed for microfluidic devices and micro-reactors, however, these still require optical access (Schembri 2011). The only micro-sensor demonstrated to date for measurement of two-phase flow in fuel cells is reported by Conteau et al. (2010). The sensor was based on an impedance measurement between two electrodes on either side of a graphite micro-channel used to simulate experimentally two phase flows relevant to fuel cells. Correlation of the sensor data with high-speed digital images showed the capabilities of the sensor in detecting small and fast water droplets injected into the microchannel.

Electrode-based sensors, such as the one developed by Conteau et al., will require special attention to electrical isolation, which, inside of an electrochemically active fuel cell, can prove difficult. For distributed measurements using these sensors, multiplexing will require several electrically isolated leads, which poses another significant instrumentation challenge.

Fiber optics is an approach to PEMFC diagnostics that is free from the constraints of electronic sensors. Important advantages of optical fiber sensors are that they are inherently small, electrochemically inert, and there is potential for multiplexing several sensors along a single optical fiber.

The fiber Bragg grating (FBG) sensor, for instance, can be multiplexed easily, and can be used to measure multiple parameters. As a result, there are growing number of applications for which FBGs are being used. FBG sensors were recently developed and used to measure temperature and humidity in operating PEM fuel cells (David et al. 2009, 2010). Humidity sensitivity is achieved by adding a hygroscopic polymer coating to the cladding of fiber.

Temperature and humidity are important parameters inside a PEMFC, but the measurement of liquid water is paramount. It has been shown that by removing the glass cladding around an FBG, it becomes sensitive to the surrounding refractive index (Iadicicco et al. 2004; Schroeder

et al. 2009; Meltz et al. 1996). These types of sensors, known as evanescent field sensors are sensitive along the length of the FBG, which make them ideal for multiplexed implementation into fuel cell plates. Such sensors have not yet, however, been demonstrated to measure the difference of refractive index between air and water inside of a PEMFC.

In this paper, a proof-of-concept study of an FBG-based evanescent field sensor for detecting water droplets in a microchannel is presented. Validation of the design was carried out by correlations between high-speed digital video footage and the sensor response under various two-phase flow conditions.

2 Sensing principle

An FBG typically consists of a short segment of single mode optical fiber with a photo-induced periodically modulated index of refraction in the core of the fiber. When the grating is illuminated with broadband light, the reflected spectrum has a peak at the Bragg wavelength given by

$$\lambda_B = 2\Lambda n_{\text{eff}}, \quad (1)$$

where n_{eff} is the effective index of refraction of the modified core and Λ is the grating pitch. Both n_{eff} and Λ are dependent on strain and temperature (Kersey et al. 1997), which enables the FBG to be used for sensing parameters such as temperature, strain, pressure and humidity.

When the cladding of the fiber is removed around the Bragg grating, n_{eff} becomes influenced by the refractive index of the surrounding medium. For constant temperature and strain conditions, small variations in the Bragg wavelength due to changes in the effective refractive can be simply expressed by

$$\Delta\lambda_B = 2\Delta n_{\text{eff}}(n_s)\Lambda \quad (2)$$

where n_{eff} is written as a function of n_s , the refractive index of the surrounding medium.

The refractive index sensitivity of etched cladding FBGs written in standard single mode fiber with a core of 8.3 μm was determined numerically and experimentally by Iadicicco et al. (2004). A non-linear dependence of λ_B on n_s was reported with increased sensitivity as the surrounding refractive index approached that of glass. The study showed that for a sensor with cladding diameter of 8.5 μm , measurement resolutions of 10^{-5} and 10^{-4} were possible for the outer refractive index of 1.45 and 1.33, respectively, when using an FBG interrogator with 1 pm resolution.

Iadicicco et al. cite the reason for higher sensitivity for higher refractive index surroundings is the penetration depth of the evanescent field. The penetration depth is the

distance from the surface over which the evanescent field intensity decays to $1/e$ of its value at the interface. It is given by Dakin (1988):

$$d_p = \frac{\lambda}{2\pi(n_1^2 \sin^2 \theta - n_s^2)^{1/2}}. \quad (3)$$

For the case of an optical fiber etched to the core, n_1 is the refractive index of the glass core, n_s is the refractive index of the surrounding medium. θ is the angle of incidence of the light at the interface, which, to be contained within the fiber by total internal reflection, must be greater than the critical angle, and λ is the free-space wavelength of the light. It is clear from Eq. 3 that the penetration depth of the evanescent field increases for higher index surroundings, which can explain the increasing sensitivity of the FBG refractive index sensors measured by Iadicicco et al.

The penetration depth can also be used to estimate the limitations in detecting films of liquid water on an etched FBG sensor. Using Eq. 3, it can be shown that in approximate terms only material located within about one wavelength of the fiber surface can interact with the the evanescent field to any extent (Dakin 1988). A typical etched FBG sensor is only sensitive to water film thicknesses up to the Bragg wavelength ($\sim 1 \mu\text{m}$), beyond which no further change in the effective index of refraction can be gained.

Etching standard single-mode optical fiber to a diameter of $\sim 8 \mu\text{m}$ makes it difficult to handle and to package into a sensor, particularly when embedding into a surface to detect liquid water. Alternative solutions to gain access to the evanescent field about an FBG without sacrificing its mechanical integrity were demonstrated by Schroeder et al. (2009) and Meltz et al. (1996). Schroeder et al. used side polishing on a pre-embedded standard single-mode fiber to construct a sensor that was sensitive to the refractive index change induced by the presence of hydrogen on the surface. Meltz et al. used a specialty D-shaped fiber supplied by KVH Industries, Inc. with minimal etching to demonstrate a highly sensitive refractive index sensor. This was the approach taken for the development of the liquid water surface sensor described in this paper.

3 Materials and methods

Based on the sensing principle described in the previous section, a liquid water sensor consisting of a D-shaped fiber embedded into the surface of a polymer was constructed. Two adjacent FBGs were used so that the size and speed of a droplet could be measured as it passes along the length of the fiber (Fig. 1). To test and evaluate performance, the sensor was embedded in a microfluidic platform allowing optical access and controlled generation of two phase flow

(air-water). While one of the target applications of the proposed sensor is two-phase flow in PEM fuel cells, the focus of this paper is a demonstration of the technique in a generic microchannel two-phase flow where experimental conditions were selected to test and demonstrate the capabilities of the sensors rather than to investigate in detail flows specific to a particular application. The sensor fabrication and testing methods are discussed in the following sections.

3.1 Sensor fabrication

Polydimethylsiloxane (PDMS) polymer was used as a substrate material for the sensor prototype because it has good adhesion to glass, and, like the graphite composite used for fuel cell plates, it is hydrophobic. In addition to these properties, PDMS is commonly used in prototyping microfluidic devices and, therefore, could be used for the transparent microchannel to test the sensor. While PDMS was well suited for the proof of concept of the technique, due to its high thermal expansion and low modulus, PDMS is not proposed as a commercially robust sensor substrate. Robust future designs will require use of epoxy substrate or other suitable materials depending on the target application.

D-fiber has a roughly semi circular cross section with the light carrying core lying just beneath the flat surface. It requires only minimal etching to access the evanescent field near the core of the fiber, leaving a fiber that is substantially easier to work with during the fabrication steps following the etching. The D-fiber used for the sensors in this study was supplied by KVH industries, Inc.

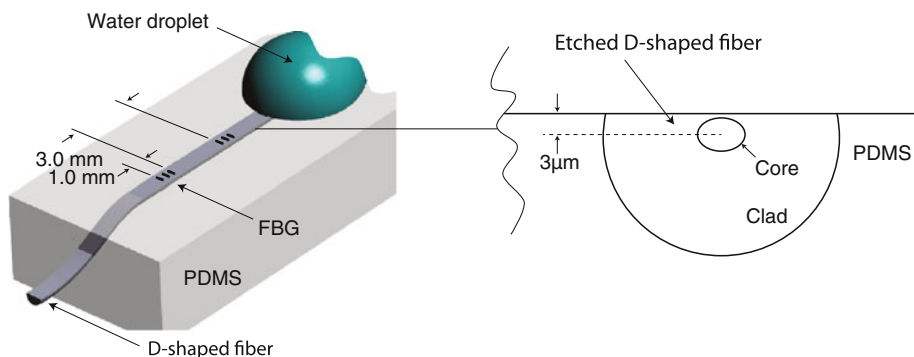
Two adjacent FBGs were written into the D-fiber by Technica SA, Inc., China. They were specified to be 1 mm in length with centre wavelengths of 1,547 and 1,552 nm and spaced apart at the inside edges by 3 mm (Fig. 1). Using a hot wire technique to locate the FBGs, the centre-to-centre grating spacing was verified to be $4 \pm 0.4 \text{ mm}$.

To detect the refractive index change above the flat side of the D-fiber, the fiber was etched with hydrofluoric acid (HF). Using a 48% HF solution at room temperature, the etch rate for the flat to the round dimension was determined to be $2.75 \mu\text{m}/\text{min}$. A length of 1.5 cm of the D-fiber containing the two FBGs at the distal end of the fiber was immersed in the HF solution and etched for 8 min.

According to the D-fiber specifications provided by KVH, Inc. the core diameter is $5 \mu\text{m}$, and the distance from the centre of the core to the flat side is nominally $\sim 14 \mu\text{m}$. After etching the D-fiber in HF for 8 min this distance becomes $3 \mu\text{m}$, leaving a cladding thickness of $\sim 0.5 \mu\text{m}$ above the core.

The spectra of the FBGs were measured prior to and after etching with a Smart Scan FBG interrogator (Smartfibers, Inc., Bracknell, UK). Wavelength resolution of the Smartscan is $\sim 1 \text{ pm}$. The full etching caused a blue

Fig. 1 Schematic of the liquid water sensor



shift of ~ 800 pm of the Bragg wavelengths when exposed to the air, with no difference in peak amplitude. This effect has been observed before, and is attributed to residual strain relaxation in the core of the fiber (Iadicicco et al. 2004).

The spectral response of the etched FBGs to liquid water was initially tested by submerging the fiber vertically in a beaker of distilled water. This method ensures that the FBGs are strain free, isolating the response to a change in refractive index. FBGs are known to have low response to hydrostatic pressure (Dennison 2008): the typical pressure sensitivity of FBGs is 3 pm/MPa allowing resolution of pressures of the order MPa. The maximum hydrodynamic pressures that the sensor would be subjected in the present experiments are of the order of 10 KPa, which would correspond to a shift of approx 0.03 pm compared to the shifts of 400 pm reported here (Fig. 4). The effect of hydrodynamic pressure is therefore negligible. Upon submersion, the Bragg wavelengths of the two FBGs increased by ~ 400 pm, indicating a clear response to the change in surrounding refractive index (Fig. 2). Recovery of the initial dry FBG spectrum was quickly achieved upon removing the fiber from the water, and wicking the micro droplets off it with a dry wipe.

Subsequent to etching the D-fiber, it was cast into PDMS using a mold made from Poly(methyl methacrylate) (PMMA). PMMA has a flat, shiny surface to which PDMS does not bond.

Using a fiber rotator, and a stereo microscope, the D-fiber was oriented in the mold such that the flat side of the fiber was parallel to the PMMA surface. A 1 cm length of the fiber containing the two FBGs was pressed against the PMMA surface with two small PDMS blocks that were weighted down. This was to ensure the FBGs would be exposed at the surface of the sensor once released from the mold.

The PDMS used for the sensor was the two part Sylgard 184 silicone elastomer kit from Dow Corning, Inc. A 5:1 by weight ratio of pre-polymer to curing agent was used to obtain a stiffer cured material. After thoroughly mixing the PDMS, it was degassed under vacuum for 20 min, and then

poured into the mold over top of the FBGs to a depth of ~ 7 mm. The PDMS was allowed to cure for 24 h.

With the FBGs located at its center, a rectangle approximately 30 x 60 mm was cut into the cured PDMS with a scalpel. The rectangular slab containing the FBGs was carefully released from the PMMA mold. Inspection under a microscope revealed a thin layer of PDMS on top of the fiber that inhibited the sensor response to liquid water. This thin layer was removed mechanically with a soft tool, and the sensitivity to surface droplets was established.

3.2 Sensor testing setup

A schematic of the setup for sensor testing is shown in Fig. 3. A microchannel made from PDMS was placed on top of the sensor allowing controlled generation of both droplet and slug two-phase flow. The cross-sectional area of the microchannel as well as the range of air and water injection rates used in the tests are representative of fuel cell conditions. The sensors performance was validated by correlating high-speed digital video of the two-phase flow with the sensor data, which was acquired synchronously.

The digital video was taken with a Vision Research, Inc. (Phantom, Miro 4) camera at a frame rate of 1,000 frames per second. The FBG data were acquired at 2 kHz using the Smartsan interrogation unit.

The microchannels used for the tests were fabricated out of PDMS using standard soft photolithography techniques and incorporated air and water injection ports connected to syringe pumps controlled to create the desired flow regime. The dimensions of the microchannel are shown in Fig. 3. The air and water injection ports were fed with syringe pumps to create segmented flow within the channel.

With air and water injection rates set to 90 and 45 $\mu\text{l}/\text{min}$ respectively, short segments of water, or slugs, spaced apart by longer segments of air passed through the channel and over the embedded FBGs. A small amount of red dye was mixed into the water as a contrast to enable better visualization of the water. The magnitude of the

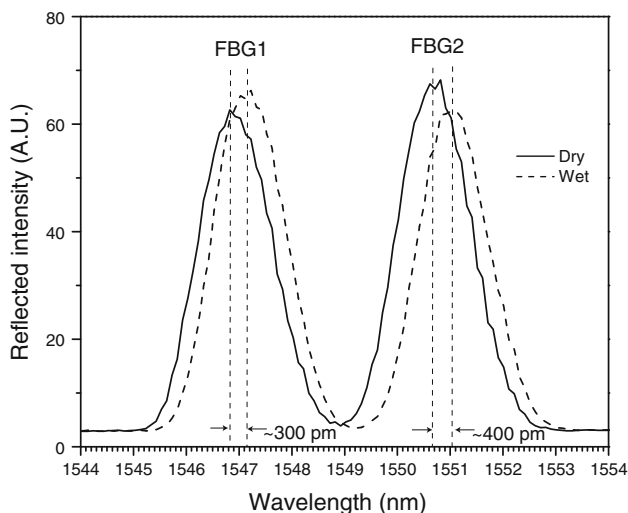


Fig. 2 Sensor response to liquid water

wavelength shift due to dyed water during microchannel testing was practically identical to the shift observed with distilled water, and the small change in the refractive index of the water with the addition of dye was therefore negligible for the purpose of the present proof of concept experiments.

To test the sensor response to fast moving droplets, a 1-mm wide PDMS channel was created with side walls and no cover. Individual droplets were deposited at the entrance to the channel. Forced air was blown through the widened entrance to the channel causing the small droplet to convect through the channel at a high speed. Care was taken to ensure the droplet remained intact without touching the side walls as it passed over the FBGs. During initial tests, repeated dipping of the sensor into liquid water showed no signs of performance degradation. Likewise, for the microchannel tests, no significant changes were observed in the response over 50 wet–dry cycles. Glass and the FBG are stable and based on our prior laboratory experience, the properties of PDMS do not change over the several cycles and timeframe of the experiments.

4 Results and discussion

Tests were carried out to validate the sensor in the slug and droplet flow regimes that are relevant to the fuel cell two-phase flows that motivated this work (Wu 2012).

4.1 Slug flow regime

In Fig. 4, the sample results representing four typical wet–dry cycles from the slug flow regime tests are shown. The slugs passed through the channel in the direction from FBG1 to FBG2. The sensor data plotted in Fig. 4a were taken over a 25 s time period during which 4 slugs passed across the sensor. It is clear that each FBG exhibits an on–off type response to the passing slugs with the response of FBG1 leading that of FBG2, which is consistent with the relative locations of the gratings. The Bragg wavelength shifts are consistent with the initial tests carried out after etching (Fig. 2).

The sensor response to the passage of a single slug is shown in Fig. 4b. Selected video frames, at particular times of interest on the response plot are shown in Fig. 4c for comparison. Comparison of the video frames to the sensor data is important for validating the sensor performance. The locations of the FBGs have been highlighted since they are normally transparent.

At time t_1 , both sensors are reading the low Bragg wavelength indicating a dry state. Looking at the first video frame, this is indeed the case, as the slug has not yet reached FBG1. At time t_2 , FBG1 is starting to respond with an increasing Bragg wavelength, indicating that it is entering into the wet state. The video frame corresponding to t_2 agrees with the data, showing the front of the slug just reaching the edge of FBG1. A short time later, at t_3 , the FBG response becomes saturated, indicating that it is fully covered by water. This is confirmed in the corresponding video frame, which shows the slug covering FBG1. The same correlation for wetting is seen for FBG2 at t_5 and t_6 .

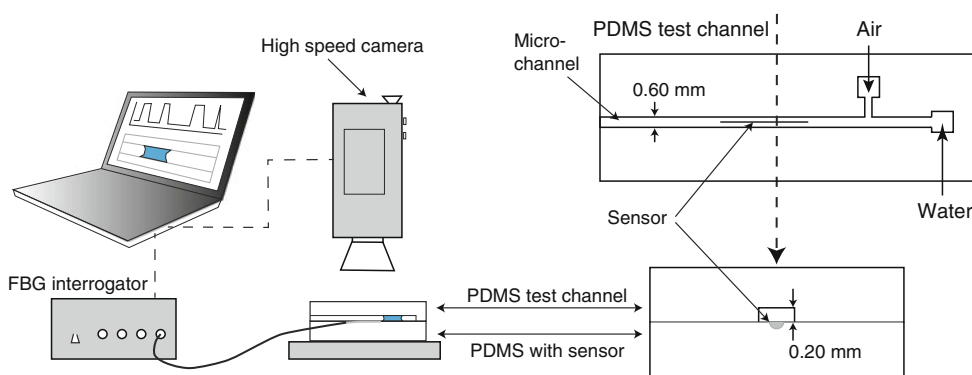
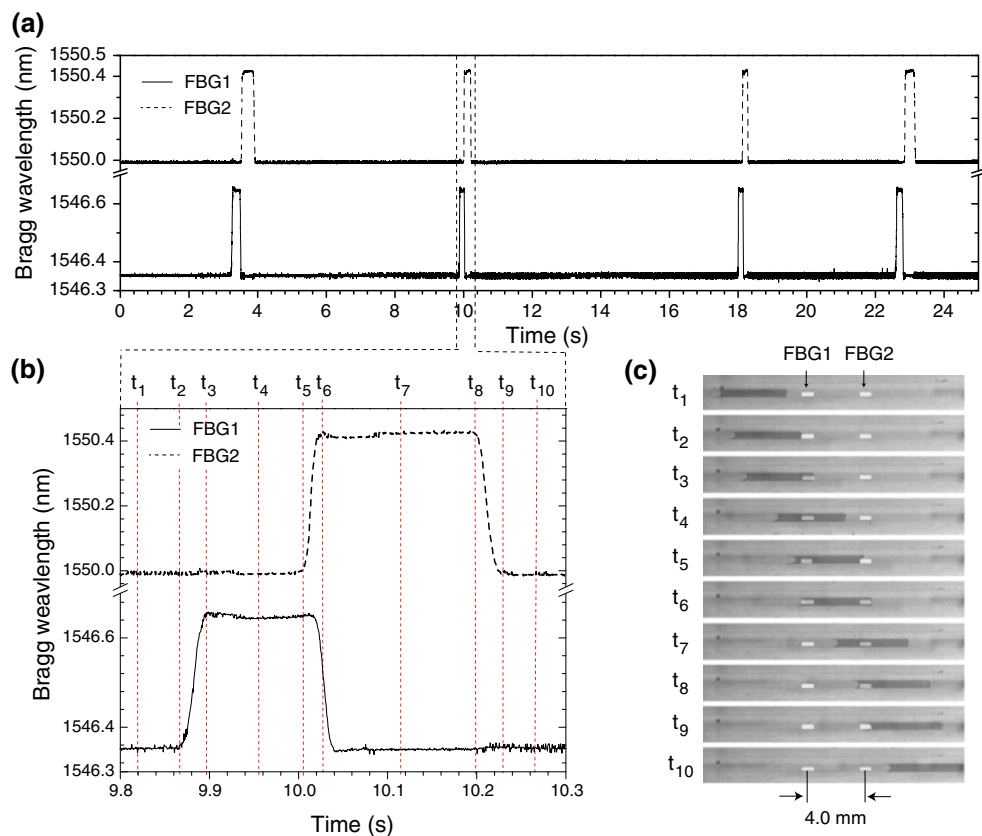


Fig. 3 Schematic of the sensor test setup

Fig. 4 Results from sensor validation test in the slug flow regime. **a** Response of sensor to passing slugs of water flowing through microchannel. **b** Bragg wavelength shifts of FBG1 and FBG2 as a result of a single slug. **c** Frames from high-speed camera corresponding to the times shown in the sensor data from plot (b). Locations of FBGs have been marked in the images



The wet to dry transition for FBG2, between times t_8 and t_9 shows an immediate recovery as soon as the trailing edge of the slug reaches the edge of the FBGs. This is an indication that there is no film of water left on the fiber behind the slug, despite a difference in wetting characteristics between the PDMS and the glass. As discussed, the evanescent field interaction is confined to a short distance above the sensor. From calculations of the penetration depth (Eq. 3), this distance can be approximated as the Bragg wavelength of the FBG. By this reasoning, saturation of the signal occurs for films that are thicker than the Bragg wavelength ($1.55 \mu\text{m}$). Intermediate thicknesses less than $1.55 \mu\text{m}$ should yield intermediate wavelength shifts, however, no such intermediate wavelength shifts were observed between the passage of slugs.

After validating the FBGs responses to the passing slug using visualization, it was clear that the data could be used to reliably calculate the average velocity of the slug as it passes over the sensor. The spacing between FBG1 and FBG2 ($4.0 \pm 0.4 \text{ mm}$) was divided by the time interval between the leading edges of the response curves of Fig. 4b, i.e. times t_2 for FBG1 and t_5 for FBG2. For this slug, the average velocity was $3.0 \pm 0.6 \text{ cm/s}$. The slug length can then be computed by multiplying the residence time on one FBG by the average velocity. The residence time, at FBG2 for example, is taken to be $t_8 - t_5 = 0.2 \text{ s}$.

With this, the size of the passing slug is estimated to be $6.0 \pm 1.0 \text{ mm}$. Using the scale on the images, the slug measures closer to 5.0 mm . For a more instantaneous measure of the slug velocity, the response of a single FBG was also analyzed. The velocity of the front passing FBG1 can be measured by dividing the FBG length by the time taken to cover it ($t_3 - t_2 = 0.029 \pm 0.005 \text{ s}$). Using an FBG length of $1.0 \pm 0.1 \text{ mm}$, the velocity is calculated to be $3.5 \pm 0.7 \text{ cm/s}$. From the residence time at FBG1, the slug length is calculated to be $5.3 \pm 1.2 \text{ mm}$. Which is in good agreement with what is measured in the image.

The accuracy of these particular velocity measurements is estimated to be 20% of the calculated velocity. This uncertainty arises from the uncertainties in the lengths of the FBGs, the distance between the FBGs and the time intervals used in the computation. The accuracy of the visualization technique used for validation is estimated to be of the same order.

The velocities of the four slugs presented in Fig. 4a were measured using the high-speed video images and the FBG data. The results of these measurements are presented in Table 1 for comparison. v_1 is the velocity measured across FBG1, v_2 is the velocity across FBG2, and v_{ave} is the average velocity measured between the FBGs. The accuracy of these particular measurements is estimated to be 20% of the measured velocity for both techniques. This

Table 1 Comparison of slug velocities measured with high-speed video analysis and FBG sensor data analysis

| | Velocity from video (cm s ⁻¹) | | | Velocity from FBGs (cm s ⁻¹) | | |
|--------|---|----------------|------------------|--|----------------|------------------|
| | v ₁ | v ₂ | v _{ave} | v ₁ | v ₂ | v _{ave} |
| Slug 1 | 1.6 ± 0.3 | 2.0 ± 0.4 | 1.7 ± 0.3 | 2.0 ± 0.4 | 2.5 ± 0.5 | 1.4 ± 0.3 |
| Slug 2 | 3.0 ± 0.6 | 4.3 ± 0.9 | 3.5 ± 0.7 | 3.5 ± 0.7 | 4.3 ± 0.9 | 3.1 ± 0.6 |
| Slug 3 | 3.3 ± 0.7 | 4.2 ± 0.8 | 3.8 ± 0.8 | 3.3 ± 0.7 | 4.8 ± 1.0 | 3.9 ± 0.8 |
| Slug 4 | 2.0 ± 0.4 | 2.1 ± 0.4 | 1.9 ± 0.4 | 1.9 ± 0.4 | 2.6 ± 0.5 | 1.9 ± 0.4 |

Slugs 1-4 correspond to those shown in Fig. 4a. The velocities v₁ and v₂ are measured across the lengths of FBG1 and FBG2, respectively, and v_{ave} is the average velocity measured over the distance between the two FBGs

arises from the uncertainties in the lengths of the FBGs, the distance between the FBGs and the time intervals used in the calculations. Overall, the two techniques showed good correlation for each of the three velocities measured for each slug. The average difference between the video measurements and the FBG measurements shown in Table 1 is 11.6%, which is well within the uncertainty of either technique. The accuracy of the FBG technique is, therefore, as good as the visualization technique, and largely dependent on the accuracy to which the lengths and spacing of the FBGs are known. While the single FBG velocity measurement technique is more expedient, flows in which the droplets/slugs are smaller than the FBG length do require data from two FBGs.

4.2 Droplet flow regime

Representative results from the passage of a single fast moving droplet over the sensor are shown in Fig. 5. As with the slug results, the response data for the droplet correlated well with the synchronized video images. The response curve of FBG1 has features that are not present in

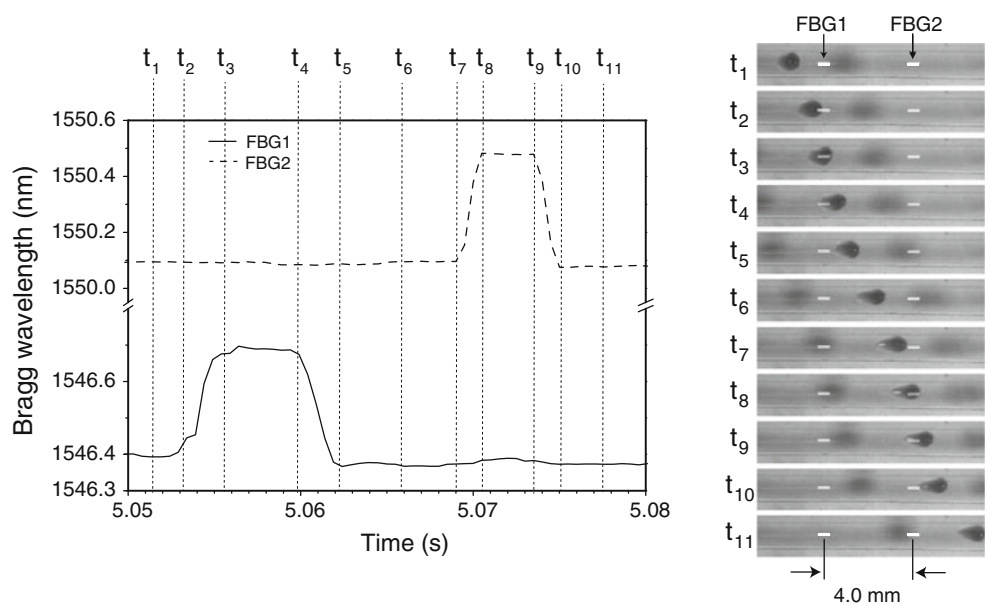
the response of FBG2. Upon closer analysis of the high-speed video, these features in the data can be attributed to the droplet front’s shape changing as it passes over FBG1. This is likely due to a combination of fluctuation from the forced air entering the open-top flow channel and imperfect homogeneity of the surface.

Using the FBG spacing and the time interval between t₂ and t₇, the average velocity of the droplet shown in Fig. 5 is calculated to be 25 cm/s. It is clear, however, from the response curves that the droplet speeds up between FBG1 and FBG2. Using the response of only FBG2, the velocity is calculated to be 53.0 cm/s, more than double the average velocity. With this, the size of the droplet is estimated to be 2.3 mm. This is in good agreement with the video frame corresponding to t₁₀.

5 Conclusions

The concept of a surface embedded FBG sensor for the measurement of two-phase flow dynamics has been demonstrated and validated. It was shown that with minimal

Fig. 5 a Sensor data from single fast droplet test. **b** Selected frames from the high-speed video, corresponding to times shown in (a). Locations of FBGs have been marked in the images



etching, FBGs written into a D-shaped fiber respond to the presence of liquid water due to a change in the surrounding refractive index.

A sensor consisting of a D-fiber with two adjacent FBGs embedded into the surface of a polymer was constructed. The polymer substrate with embedded sensor was used as a wall in a microchannel. High speed digital video of the droplet flow was captured synchronously with the sensor data acquisition. The FBGs exhibited an on–off type response to the passage droplets, which correlated precisely with liquid water flowing over the FBG locations. This correlation enabled the measurement of droplet average velocity and size using only the sensor data. In addition to the use of both FBG signals for the purpose of measuring droplet speed and size, it was shown that for droplets larger than the FBG length, a single FBG can be used to estimate the speed and size of a fast moving droplet with accuracy that is comparable to the visualization technique used for validation.

Testing of this sensor concept was carried out under conditions of constant temperature and no applied stress. For temperature compensation, it is suggested that a co-located and in situ calibrated FBG be used. In applications where it is necessary to limit perturbations due to strain, a stiffer epoxy substrate material is suggested rather than PDMS.

The study presented here suggests that an evanescent field FBG sensor based on this concept could be adapted for use in the flow-channel of a PEMFC to investigate droplet and flooding phenomena. In future work, we will use these sensors for detailed analysis of two phase flows specific to fuel cells, which involve fibrous hydrophobic surfaces (gas diffusion layers). Further sensor development will also be undertaken to distinguish between flow regimes that exist within the microchannels of a fuel cell. This sensing concept is not, however, limited to fuel cells. It could be applied, for example, to microfluidic devices or to the detection of condensation.

Acknowledgments This research was funded through a Strategic Research grant from the Natural Sciences and Engineering Research Council (NSERC) of Canada. The D-fiber used for the sensors in this study was kindly provided by KVH industries Inc.

References

- Bazyalak A (2009) Liquid water visualization in PEM fuel cells: a review. *Int J Hydrogen Energy* 34:3845
- Bergles AE, Kandlikar SG (2005) On the nature of critical heat flux in microchannels. *J Heat Transf* 127:101
- Conteau D, Bonnet C, Funfschilling D, Weber M, Didierjean S, Lapique F (2010) Detection of liquid water in pem fuel cells'

- channels: design and validation of a microsensors. *Fuel Cells* 4:520
- Dakin J, Culshaw B (1988) *Optical fiber sensors: principles and components*. Artech House Inc., Norwood
- David NA, Wild PM, Hu J, Djilali N (2009) In-fibre Bragg grating sensors for distributed temperature measurement in a polymer electrolyte membrane fuel cell. *J Power Sour* 192:376. doi: [10.1016/j.jpowsour.2009.03.021](https://doi.org/10.1016/j.jpowsour.2009.03.021)
- David NA, Wild PM, Jensen J, Navessin T, Djilali N (2010) Simultaneous in situ measurement of temperature and relative humidity in a PEMFC using optical fiber sensors. *J Electrochem Soc* 157(8):B1173. doi: [10.1149/1.3436652](https://doi.org/10.1149/1.3436652)
- Dennison C, Wild P (2008) Enhanced sensitivity of an in-fibre bragg grating pressure sensor achieved through fibre diameter reduction. *Meas Sci Technol* 19:125301
- Funfschilling D, Ma Y, Li HZ (2010) Scaling the formation of slug bubbles in microfluidic flow-focusing devices. *Microfluid Nanofluid* 8:467
- Gunther A, Khan S, Thalman M, Trachsel F, Jensen K (2004) Transport and reaction in microscale segmented gas-liquid flow. *Lab Chip* 4:278
- Hetsroni G, Mosyak A, Segal Z (2002) A uniform temperature heat sink for cooling of electronic devices. *Int J Heat Mass Transf* 45:3275
- Iadicco A, Cusano A, Cutolo A, Bernini R, Giordano M (2004) Thinned fiber bragg gratings as high sensitivity refractive index sensors. *IEEE Photo* 16:1149
- Kersey A, Davis M, Patrick H, LeBlanc M, Koo K, Askins C, Putnam M, Friebele EJ (1997) Fiber grating sensors. *J Lightwave Technol* 15:1142
- King RGC, Walsh E (2007) Piv measurements of flow within plugs in a microchannel. *Microfluid Nanofluid* 3:463
- Li H, Tang Y, Wang Z, Shi Z, Wu S, Song D, Zhang J, Faith K, Zhang J, Wang H, Liu Z, Abouatallah R, Mazza A (2008) A review of water flooding issues in the proton exchange membrane fuel cell. *J Power Sour* 178:103
- Meltz G, Hewlett SJ, Love JD (1996) In: *Proceedings of SPIE*, vol 2836. Chemical, biochemical, and environmental fiber sensors VIII, pp 342–350
- Waelchli S, Von Rohr PRO (2006) Two-phase flow characteristics in gas-liquid microreactors. *Int J Multiph Flow* 32:791
- Schembri MBF (2011) Periodic input flows tuning nonlinear two-phase dynamics in a snake microchannel. *Microfluid Nanofluid* 11:189
- Schroeder K, Ecke W, Willsch R (2009) Optical fiber bragg grating hydrogen sensor based on evanescent-field interaction with palladium thin-film transducer. *Opt Lasers Eng* 47:1018
- Tibiri GRB, do Nascimento FJ (2010) Film thickness measurement techniques applied to micro-scale two-phase flow systems. *Exp Thermal Fluid Sci* 34:463
- Wu TC, Djilali N (2012) Experimental investigation of water droplet emergence in a model PEMFC cathode microchannel. *J Power Sour* (submitted)
- Zhang L, Koo JM, Jiang Lea (2002) Measurements and modeling of two-phase flow in microchannels with nearly constant heat flux boundary conditions. *J Microelectromech Syst* 11:12
- Zhu X, Sui PC, Djilali N (2008) Numerical simulation of emergence of a water droplet from a pore into a microchannel gas stream. *Microfluid Nanofluid* 4:543–555
- Zhu X, Sui PC, Djilali N (2008) Three-dimensional numerical simulations of water droplet dynamics in a PEMFC gas channel. *J Power Sour* 181:101